

# Feature Extraction Techniques in Remote Sensing Images: A survey on Algorithms, Parameterization and Performance

Edmore Chikohora, Obeten O. Ekabua

**Abstract:** Remote Sensing Images (RSI) employs various Feature Extraction Techniques (FET) that implement different algorithms to extract features from a query image. In this paper, we provide a critical and comprehensive survey on algorithms implemented by different FET, their parameter selection strategies and performance. The survey is divided into three parts where initially three FET are selected and the algorithms they implement are analysed. Secondly, their parameter selection strategies are surveyed and finally a critical analysis on performance based on literature results obtained is provided with some concluding remarks.

**Key words:** Remote Sensing, Feature Extraction, Convolution Mask, Mahalanobis Distance, Gaussian Envelope, Frequency Harmonic.

## I. INTRODUCTION

Remote Sensing (RS) is the science of deriving information about a feature, an object or a phenomenon from a distance by analysing the energy reflected or emitted by the feature [1]. The main energy detected by remote sensing systems is electromagnetic energy. RS uses sensors to measure the amount of electromagnetic energy exiting an object or a geographic area.

The sensors are characterized by different resolutions such as spatial, spectral, radiometric and temporal. It can be noted that objects and features on the earth's surface interact differently with the electromagnetic energy based on their molecular composition and the differences in the amount and properties of electromagnetic radiation becomes a valuable source of information.

RS imagery finds its application spanning over quite a number of domains and these include mapping land-use and cover, agriculture, soils mapping, forestry, city planning, archaeological investigations, military observation and geomorphologic surveying among other uses [2]. For example, back in the late 1970s and early 1980s, a great research effort was focused on the use of multispectral images (obtained through RS) for crop inventory and crop production. The Large Area Crop Inventory Experiment (LACIE) demonstrated the feasibility of utilizing satellite-based multispectral data for estimation of wheat production based on techniques that are still in use today by crop production forecasters in the USDA Foreign Agricultural Service [3].

The rest of the paper is organised as follows: section 2 provides a summary of related work and algorithms in form of figures and formulae.

### Manuscript Received on March, 2014

**Edmore Chikohora**, Department of Computer Science North-West University, Mafikeng Campus Private Bag X2046, Mmabatho 2735, South Africa.

**Obeten O. Ekabua**, Department of Computer Science North-West University, Mafikeng Campus Private Bag X2046, Mmabatho 2735, South Africa.

Section 3 reviews parameter selection strategies that are employed by different FET, while section 4 provides a critical analysis on performance of algorithms based on literature reviewed and section 5 concludes the paper.

## II. RELATED WORK SUMMERY

This chapter reviews some related work on different FET as viewed by different authors.

### 2.1 Traditional Gabor Filter

Daugman [2] discussed the Traditional Gabor Filter (TGF) as a technique that implements one or multiple convolutions of an input image with a 2-D Gabor Function. The function was viewed as a harmonic oscillator composed of sinusoidal plane wave of a particular frequency and orientation within a Gaussian envelope. The TGF views a complex 2-D filter over the image domain (x,y) as;

$$G(x, y) = \exp\left(\frac{(x-x_0)^2}{2\sigma_x^2} - \frac{(y-y_0)^2}{2\sigma_y^2}\right) \exp(-2\pi i(u_0(x - x_0) + v_0(y - y_0))) \quad (1)$$

where  $(x_0, y_0)$  specify the location in the image  $(u_0, v_0)$ , specifying modulation that has spatial-frequency  $w_0 = \sqrt{u_0^2 + v_0^2}$  and orientation  $\phi = \arctan\left(\frac{u_0}{v_0}\right)$ . While  $\sigma_x$  and  $\sigma_y$  are the standard deviations of the Gaussian envelope along the x-axis and y-axis respectively [4].

The real part of the filter is specified based on formula (1) as;

$$Re\ g(x, y; T, \phi) = \exp\left(-\frac{1}{2} \left[\frac{x^2}{\sigma_x^2} + \frac{y^2}{\sigma_y^2}\right]\right) \cos\left(\frac{2\pi x \phi}{T}\right) \quad (2)$$

where  $x_\phi = x \cos \phi + y \sin \phi$  and  $y_\phi = -x \sin \phi + y \cos \phi$ .

In (2),  $\phi$  is the orientation of the TGF,  $T$  is the period of the sinusoidal plane wave and  $\sigma$  is the standard deviation along the axis as mentioned earlier. Further decomposing (2) result in the formation of two orthogonal parts. That is, one parallel while the other will be perpendicular to the orientation  $\phi$  and this would be represented as;

$$Re\ g(x, y, T, \phi) = h_x(x; T; \phi) \cdot h_y(y; \phi) \\ \left\{ \exp\left(-\frac{x_\phi^2}{2\sigma_x^2}\right) \cos\left(\frac{2\pi x_\phi}{T}\right) \right\} \cdot \left\{ \exp\left(-\frac{y_\phi^2}{2\sigma_y^2}\right) \right\} \quad (3)$$

### 2.2 Modified Gabor Filter (MDF)

The MDF as discussed in [4], replaces the cosine function  $\cos(x; T)$  in (3) with a periodic function  $F(x; T_1; T_2)$ , to help reduce loss of useful original information resulting from failure by the TGF to pass the entire frequency harmonic through the filter. The period  $T$  was extended to periods  $T_1$  and  $T_2$  representing the regions

above and below the axis respectively as illustrated in figure 1.

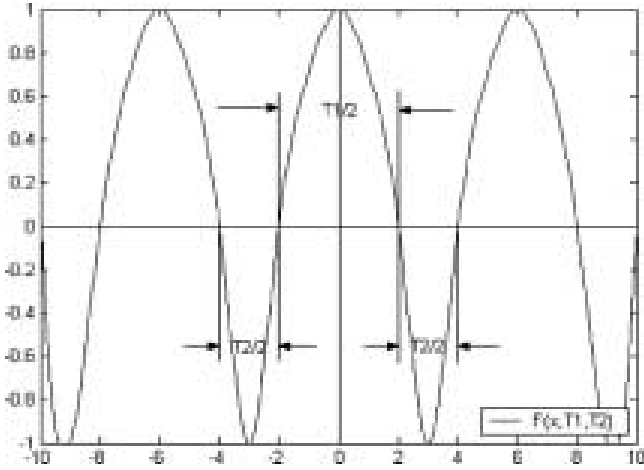


Figure 1: The periodic function  $F(x; T_1; T_2)$  with cosinusoidal functional curve with periods  $T_1$  and  $T_2$  [4] Modulating the periodic function  $F(x; T_1; T_2)$  by a Gaussian function, result in formula (3) expanding as follows;

$$g'(x, y, T_1, T_2, \phi) = h'_x(x; T_1, T_2; \phi) \cdot h'_y(y; \phi) = \left\{ \exp\left(-\frac{x_0^2}{2\sigma_x^2}\right) F(x_0, T_1, T_2) \right\} \cdot \left\{ \exp\left(-\frac{y_0^2}{2\sigma_y^2}\right) \right\} \quad (4)$$

### 2.3 Mathematical Morphology (MM)

The MM approach is based on set theoretical principles where the parameter of the morphological operations is a shape (set or function of any dimensions) commonly known as the Structuring Element (SE) [5].

The approach works by making a direct and figurative relationship between the original image to be processed and the SE using a combination of two basic operations, which are *erosion* and *dilation*. Each SE has a shape which can be thought of as a parameter to the operation and if the SE is appropriately selected with consideration to its size, shape and orientation then the operation is guaranteed of a better output image.

The two operations (erosion & dilation) are implemented using set theory which when applied to an image it result in either increasing or decreasing the intensity of the pixels. For example in [6], dilation was defined as the maximum value in the window which improves the intensity of the resulting image by changing pixels with values “0” to “1”. In that case, dilation of a grey-scale image  $F(x, y)$  by a grey-scale SE  $B(s, t)$  is denoted by;

$$(F \oplus B)(x, y) = \max\{F(x - s, y - t) + B(s, t)\} \quad (5)$$

While on the other hand, erosion is seen as just the opposite of dilation (minimum value in the window), whereby the image after erosion will be darker than original image as the pixels with value of “1” will be turned to “0” and is denoted by;

$$(F \ominus B)(x, y) = \min\{F(x + s, y + t) - B(s, t)\} \quad (6)$$

The MM approach was successfully applied on edge detection using multi-structure elements. This was meant to achieve an objective evaluation on sets of brain and chest CT images [6].

Figure 1 shows a flowchart of the Matlab simulator that was used for edge detection.

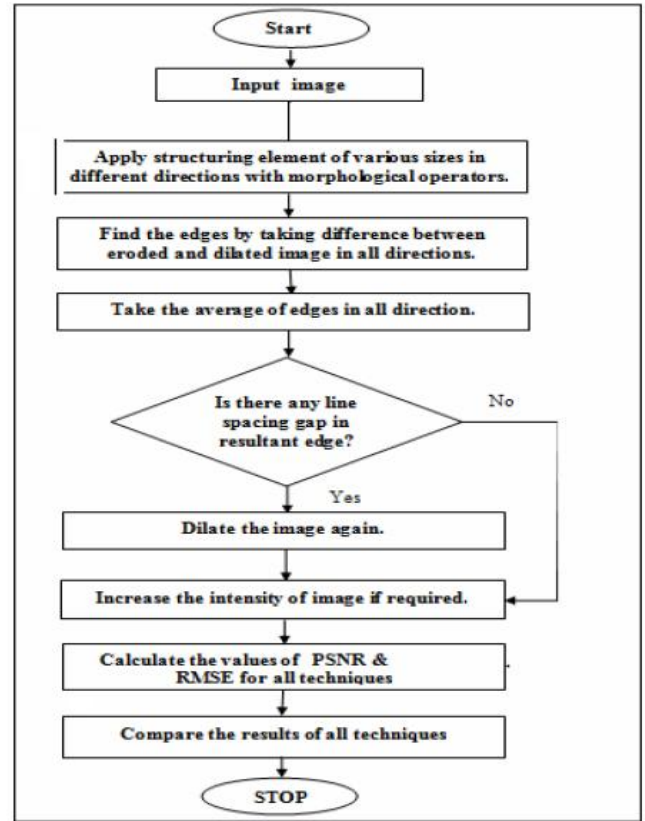


Figure 2: A Matlab flowchart for the Morphological Edge Detection Algorithm [6]

### III. PARAMETER SELECTION STRATEGIES

Parameter selection plays a crucial role in the use of FET, as the choice of “good” parameters gives a “good” output image. This section brings an overview of the parameter selection strategies employed by various FET that were discussed in section 2.

#### 3.1 The Traditional Gabor filter

A strategy that selects filter parameters semi-automatically using the Information Diagrams (ID) concept was explored in [3]. The strategy considered only the orientation ( $\phi$ ), aspect ratio ( $\gamma$ ) and sigma of the Gaussian envelope ( $\sigma$ ) while the rest of the parameters remained fixed and were specified based on empirical data [4]. The three parameters were selected by looking for a local extrema. For example, for each  $\phi$  in the set we compute the parameters of the highest local maximum and smallest local minimum as follows:

Highest Local Maximum:

$$(\sigma_i^{\max}, \gamma_i^{\max}) = \arg \max_{\sigma, \gamma} \phi - ID_{x, y}^{\phi_i} \quad (7)$$

Smallest Local Minimum:

$$(\sigma_i^{\min}, \gamma_i^{\min}) = \arg \min_{\sigma, \gamma} \phi - ID_{x, y}^{\phi_i} \quad (8)$$

From 3 and 4, the set of chosen GF parameter will be:

$$P_{\phi}^{\min} = \{(\sigma_i^{\min}, \gamma_i^{\min}, \phi_i), \dots, (\sigma_n^{\min}, \gamma_n^{\min}, \phi_n)\} \quad (9)$$

and

$$P_{\phi}^{\max} = \{(\sigma_i^{\max}, \gamma_i^{\max}, \phi_i), \dots, (\sigma_n^{\max}, \gamma_n^{\max}, \phi_n)\} \quad (10)$$

Consequently, the selected feature vector representation becomes:

$$v_{(x,y)} = (v_{(x,y)}^1, \dots, v_{(x,y)}^i, \dots, v_{(x,y)}^m)^T \quad (11)$$

Where,

$$v_{(x,y)}^i = |G_{\theta_i, \lambda_i, \sigma_i}(x, y)|, (\lambda_i, \theta_i, \sigma_i) \in P_{\theta}^{\max} \cup P_{\theta}^{\min} \quad (12)$$

Table 1 shows parameter values for  $\theta, \sigma$  and  $\gamma$  computed for each ID, the distance metrics (Euclidean & Mahalanobis) and the feature model type (magnitude versus real-imaginary parts).

Test ID	type	# local max	# local min	distance	mag	re+im
1	$\theta$	1	1	Mah	68.49	78.33
2	$\theta$	2	0	Mah	85.92	95.83
3	$\gamma$	2	0	Mah	58.19	74.16
4	$\gamma$	1	1	Mah	54.41	75.83
5	$\sigma$	2	0	Mah	58.19	72.50
6	$\sigma$	1	1	Mah	50.21	72.50
7	$\theta$	1	1	Euc	31.93	85
8	$\theta$	2	0	Euc	38.87	87.5
9	$\gamma$	2	0	Euc	17.86	53.33
10	$\gamma$	1	1	Euc	15.55	45
11	$\sigma$	2	0	Euc	24.79	74.17
12	$\sigma$	1	1	Euc	15.97	75.83

Table 1: Computed values for parameters  $\theta, \gamma, \sigma$  using Information Datagrams [3]

### 3.2 The Modified Gabor filter

Yang et al. [4] in their publication used an approach whereby the period  $T$  of the GF was decomposed into  $T_1$  and  $T_2$  and then specified the remaining parameters  $\theta, \sigma_x$  and the convolution mask size adaptively.

#### 3.2.1 Specifying Orientation $\theta$

The original image is divided into blocks of sizes  $W \times W$  and the parameter  $\theta$  is specified as the orientation of each pixel in the block using the following formula;

$$\theta(i, j) = \frac{1}{2} \tan^{-1} \left( \frac{\sum_{u=i-w/2}^{i+w/2} \sum_{v=j-w/2}^{j+w/2} 2G_x(u, v)G_y(u, v)}{\sum_{u=i-w/2}^{i+w/2} \sum_{v=j-w/2}^{j+w/2} (G_x^2(u, v) - G_y^2(u, v))} \right) \quad (13)$$

Where  $W$  is the size of each subdivided block,  $G_x$  and  $G_y$  is the local gradient at each pixel in each subdivided block. The resulting orientation value of  $\theta(i, j)$  obtained from (13) is later regularised into the range  $[-\frac{\pi}{2}, +\frac{\pi}{2}]$ .

#### 3.2.2 Specifying Standard Deviations $\sigma_x$ and $\sigma_y$

The two parameters  $\sigma_x$  and  $\sigma_y$  were specified differently owing to their effects on the output image. In [4]  $\sigma_y$  was empirically set to 4.0 and  $\sigma_x$  was of great concern as its performance is related to the periods  $T_1$  &  $T_2$  thereby influencing the degree of contrast on an image. As a result, the periodic function represented by  $h_x(x; T_1, T_2; \theta)$  formula (4) had to be examined for constraints on regions below the x-axis and those close to the origin above the x-axis.

The values of  $T_1$  &  $T_2$  were computed as in 3.2.3. Period  $T_2$  was subdivided into a smaller range each time  $T_1$  is small. Table 1 (circled) shows some of the  $\sigma_x$  results obtained from the experiments.

$T_1$	$T_2$	$\sigma_x$
4	[4, 12]	1.5
4	[14, 18]	1.6
4	[20, 28]	1.8
6	—	1.8
8	—	2.5
10	—	2.7
12	—	3.0
14	—	3.5
16	—	4.0

Table 2: Computed  $\sigma_x$  values for different  $T_1$  &  $T_2$  periods [4].

#### 3.2.3: Specifying periods $T_1$ and $T_2$

By analysing figure 1, we can infer that function  $F(x; T_1; T_2)$  is a periodic even-symmetric oscillator with the period  $(T_1 + T_2)/2$ , given that from the figure  $\frac{T_1}{2}$  and  $\frac{T_2}{2}$  corresponds to the regions above and below the x-axis respectively.

The periods  $T_1$  and  $T_2$  were specified by initially identifying a pixel that needs to be filtered, say,  $P_a(x, y)$  and noting its colour intensity. This was followed by continuously checking the neighbouring pixels until you find a pixel with different colour intensity and denote it  $P_b(x_1, y_1)$ .

$T_1$  was set to  $2W_1$  the distance between  $P_a(x, y)$  and  $P_b(x_1, y_1)$  while  $T_2$  was set to  $2W_2$ , that is, the distance between  $P_b(x_1, y_1)$  and the next pixel  $P_c(x_2, y_2)$  with a colour intensity different from  $P_b(x_1, y_1)$ . Figure 3 shows how the periods  $T_1$  and  $T_2$  were calculated on a fingerprint image obtained from an image database [4].

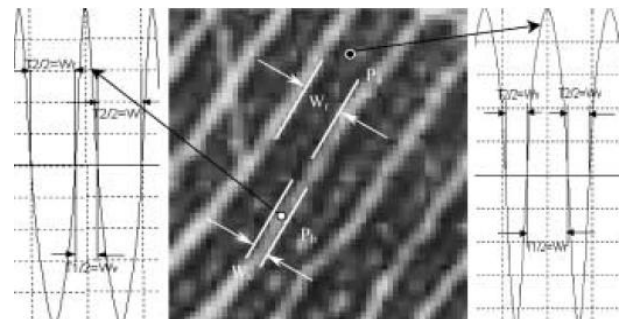


Figure 3: The Curve of  $F(X; T_1; T_2)$  Corresponding To Different Periods  $T_1$  and  $T_2$  [4]

### 3.3 The Mathematical Morphology

Given that the parameter of the morphological operations is a set or a function of any dimensions known as the SE, Fejes and Vaida in [5] used an adaptive approach to define the SE and its regions.

The approach applied a technique that was based on the method of the Least Mean Square (LMS) which minimizes the error calculated between the output and a selected desired signal (Mean Square Error).

According to the LMS coefficients-update, the following equation was used on simple grey scale dilation.

$$b'_m = b_m + 2\mu(d - y) \text{ and } b'_i = b_i \quad (14)$$

Where  $i, m \in B$  and  $m \neq i$ .  $B$  represent the support of the SE.  $b_i$  and  $b_m$  are parameters to be optimized,  $\mu$  stands for the convergence parameter,

while  $y$  and  $d$  denote the output and the reference signal respectively [5].

On the other hand a statistical analysis of the SE templates  $B_i$  was used to define the regions of interest as follows;

$$B = \{B_i\} \quad (15)$$

Then try to find tuples  $(R_k)$  of parameter locations in an arbitrary  $B_i$  template so that a value  $B_{pi}$  of  $B_i$  at location  $p$  does not differ from another element of the same tuple more than an error limit of  $\lambda$  for all  $i$ . That is;

$$\forall p, q \in R_k^\lambda, \text{ iff } \forall i \delta_{pqi} < \lambda \quad (16),$$

$$\text{where } \delta_{pqi} = (b_{pi} - b_{qi})^2.$$

As for adaptation, the coefficient-update for parameter regions was determined by identifying an element  $m$  such that, if  $m \in R_k^\lambda$  then  $r'_k = r_k + 2\mu(d - y)$  (17),

where  $r_k$  and  $r'_k$  denote the old and the new value of the  $k^{th}$  parameter region respectively and  $r'_k$  is obtained from all single parameters located in that region.

#### IV. ANALYSIS ON PERFORMANCE OF ALGORITHMS

In this section we review some experiments that were done to give an analysis on the performance of different FET discussed in section 2.

Firstly, the TGF and MGF as discussed in [4] were analysed using some fingerprint images extracted from an image database captured using an optical live-scanned equipment. The tests made a comparative analysis on the robustness and efficiency of the algorithms.

The experimental results reviewed showed a great improvement on the quality of the output image for the MGF. This could be attributed to an improved parameter selection strategy of the MGF as compared to the TGF.

##### 4.1 Testing for robustness

Figure 4(a) shows an original fingerprint image taken from the database, while 4(b) and 4(c) are the results obtained using the TGF with the values  $\sigma_x = 2.0$  and  $\sigma_x = 2.5$  respectively. These figures represent the best parameter values obtained using the TGF approach. Parameter  $\sigma_y$  was empirically assigned a fixed value of 4.0 throughout the experiments on both approaches.



Figure 4: Enhancement Results Corresponding To The Fingerprint Image (a) [4].

While 4(d) shows the resulting fingerprint image obtained using the MGF. By mere looking at the fingerprint images, it is evident that the Mahalanobis distance between (a) and (d) is almost insignificant as compared to (a) and (b) or (c)

##### 4.2 Testing for efficiency

A Pentium 4 machine with a 1.3 GHz processor speed and 128 Mb of RAM was used to test the processing time (in seconds) for both algorithms. Different image resolutions were selected for each test run with a fixed  $\sigma_y$  value of 4.0 as previously stated and a convolution of 11 for the TGF as shown in table 3.

Although the results in table 3 show a slightly higher average computational cost for the MGF in each test run (circled), this can be attributed to a larger MGF convolution mask of  $(\frac{T_2}{2} + \frac{T_1}{2} + \frac{T_2}{2})$  as compared to the TGF of  $(2N +$

1). Using a larger mask size gives an added advantage in that errors emanating from the effects of noise are reduced by local averaging within the neighbourhood of the mask.

Image resolution (pixel)	TGF ( $N = 5, \sigma_y = 4.0$ )	Average time cost (s)	
		TGF	MGF
224 × 288	1.8	0.90	0.92
256 × 256	1.8	0.94	1.01
364 × 256	2.0	1.13	1.22
400 × 376	2.2	1.76	1.89

Table 3: Comparison of time cost (in seconds) between the TGF and MGF [4]

Secondly, the performance of MM based algorithms as discussed in [7] was analysed using a well-known corrupted image called *Lena*.

The tests were carried out by making a comparative analysis of the probabilities of the pixels that were correctly detected against those wrongly detected by the algorithm.

##### 4.3 Testing for efficiency (MM algorithms)

The efficiency ( $\gamma$ ) of the detectors that implements the algorithms is calculated using the following formula;

$$\gamma = (1 - \alpha) \times (1 - \beta) \quad (18),$$

Where  $\alpha$  is the probability of corrupted pixels that were missed and  $\beta$  being the probability of pixels that were falsely detected. Form (18), we can conclude that efficiency in this case, is measured as the product of the probabilities of corrupted pixels that were detected with the pixels that were correctly detected using the algorithms.

size of $b$	3×3	3×3	3×3	5×5	5×5	5×5	7×7	7×7	
$T$	0	100	200	0	100	200	0	100	
$M$	$\alpha$	0.0000	0.1020	0.3820	0.0000	0.0031	0.0152	0.0000	0.0000
$R$	$\beta$	0.2743	0.1476	0.0163	0.0044	0.0037	0.0004	0.0001	0.0001
$D$	$\gamma$	0.7257	0.7655	0.6079	0.9956	0.9932	0.9844	0.9999	0.9999

Table 4: Effects of the size of the SE on output image [7]

Table 4 shows the effects on the size of a chosen structuring element  $b$  to the overall quality of the image being extracted. For example, the circled columns show efficiency values of 0.9999 and 0.6079 corresponding to the 7x7 and 3x3 SE respectively. The larger the SE the better output image produced as the probability value of 0.9999 is evident that the output image is almost the same as the original image which has a probability value of 1.

##### 4.4 Testing for robustness (MM algorithms)

Further experiments were reviewed which tested the robustness of the MM algorithm, the *Open-Close Sequence (OCS) algorithm* with other algorithms that are used in nonlinear filtering techniques such the Pixel-Wise Morphological Anomaly Detector (PWMAD), Network Adaptive Switching Median (NASM) and the Standard 5x5 Median.

From figure 5 it can be seen that the OCS performed robustly across all the noise ranges from 10% to 80%. The rest of the algorithms fell abruptly as the noise ration went above 40%. This is evident that the rest of the

algorithms reviewed are able to produce meaningful results only on slightly corrupted images.

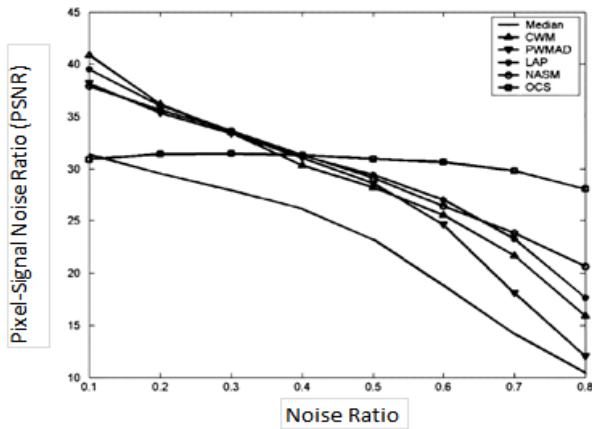


Figure 5: PSNR values for different filter algorithms operating on the image "Lena" [7].

## V. CONCLUSION AND FUTURE WORK

The paper looked at different feature extraction techniques that are used in remote sensing systems. Particular attention was on the algorithms they implement, their parameter selection strategies and performance. A comparative study of the algorithms' efficiency and robustness was covered based on the results of the experiments reviewed.

Based on the results obtained of the different experiments reviewed, it can be seen that parameter selection plays a crucial role in the use of FET if we are to get better results.

Future work focuses on parameterisation of FET by way of adaptation using evolutionary computing approaches of which genetic algorithms and neural networks shall be considered.

## REFERENCES

1. Henrique Momm and Greg Easson, Feature Extraction from High-Resolution Remotely Sensed Imagery using Evolutionary Computation. Mississippi, USA: Prof. Eisuke Kita, 2011.
2. J.G Daugman, "Uncertainty relations for resolution in space, spatial frequency, and orientation optimized by two-dimensional visual cortical filters," Optical Society of America, vol. 2, pp. 1160-1169, 1985.
3. P Moreno, A Benardino, and J Santos-Victor, "Gabor Parameter Selection for Local Feature Detection," in IBPRIA 2nd Iberian Conference on Pattern Recognition and Image Image Analysis, Portugal, 2005.
4. J Yang, L Liu, T Jiang, and Y Fan, "A modified Gabor Filter Design Method for Fingerprint Image Enhancement," Pattern Recognition Letters, no. 24, pp. 1805 - 1817, January 2003.
5. S Fejes and F Vaida, "Simplified Adaptive Approach To Efficient Morphological Image Analysis," 2004.
6. E Saffor and A Salama, "Objective Evaluation of Mathematical Mophology Edge Detection on Computed Tomography (CT) Images," International Journal of Medical Science and Engineering, vol. 7, no. 9, pp. 631 - 635, 2013.
7. D Ze-Feng, Y Zhou-Ping, and X You-Lun, "High Probability Impulse Noise-Removing Algorithm Based on Mathematical Morphology," IEEE Signal Processing Letters, vol. 14, no. 1, pp. 31-34, January 2007.
8. G Joseph, Fundamentals of Remote Sensing, 2nd edition. India: Universities press private Ltd., 2005.
9. M.S Moran, Y Inoue, and Barnes E.M, "Opportunities and Limitations for image-based Remote Sensing in Precision Crop Management.," Remote Sensing environment, vol. 61, pp. 319 - 346, January 1997.
10. Pesaresi, Kolbeinn A Benediktsson J.A, "Classification and Feature Extraction for Remote Sensing Images from Urban Based on Morphological Transformations," IEEE Transactions on Geo-Science and Remote Sensing, vol. 41, no. 9, September 2003.
11. Lee C., "Feature Extraction Based on Decision Boundaries," IEEE Trans. Pattern Anal. Machine Intell, vol. 15, pp. 388-400, April 1993.

12. Suruliandi A. Jeyabharathi D., "Perfomance Analysis of Feature Extraction and Classification Techniques in CBIR," International Conference on Circuits, Power and Computing Technologies, pp. 1211 - 1214, 2013.
13. Mehta K., Arora S. Basal A., "Face Recognition using PCA and LDA Algorithms ,," Advanded Computing and Communication Technologies (ACCT), Jan 2012.